Journal of Computational Neuroscience (2020) 48:1–20
https://doi.org/10.1007/s10827-019-00734-4

Spatiotemporal model of tripartite synapse with perinodal astrocytic process

Jhunlyn Lorenzo[1,2] · **Roman Vuillaume**[1] · **Stéphane Binczak**[1] · **Sabir Jacquir**[1,3]

Received: 9 June 2019 / Revised: 11 October 2019 / Accepted: 21 October 2019 / Published online: 3 December 2019

Abstract

Information transfer may not be limited only to synapses. Therefore, the processes and dynamics of biological neuron-astrocyte coupling and intercellular interaction within this domain are worth investigating. Existing models of tripartite synapse consider an astrocyte as a point process. Here, we extended the tripartite synapse model by considering the astrocytic processes (synaptic and perinodal) as compartments. The scattered extrinsic signals in the extracellular space and the presence of calcium stores in different astrocytic sites create local transient $[Ca^{2+}]$. We investigated the Ca^{2+} dynamics and found that the increase in astrocytic intracellular $[Ca^{2+}]$ enhances the probability of neurotransmitter release. However, the period in which the extrasynaptic glutamate lingers in the extracellular space may cause excitotoxicity. We propose further biological investigation on intercellular communication, considering that unconventional sources (nonsynaptic) of glutamate may improve information processing in neuron-astrocyte networks.

Keywords Biological model · Calcium dynamics · Compartmentalization · Extrasynaptic transmission · Perinodal astrocytic process · Plasticity · Tripartite-synapse

1 Introduction

Neural circuits, which are complex connections of integrating cells, control brain functions such as cognition, sensory, and motor skills by modulating and combining intrinsic and extrinsic signals. The neuron converts the incoming stimulus that is above its threshold into information by modulating and firing action potentials (APs). This information, encoded via frequency variation and patterns of repetitive firing, is then sent to the brain, through a neuronal network, for signal processing and response generation (Namazi and Kulish 2013; Fletcher 2016). The hippocampus is crucial for information storage and memory functions (English et al. 2017; Pissadaki et al. 2010; Vizi and Kiss 1998), and recently, astrocytes are hypothesized to impact contextual memory in the CA1 region (Choi et al. 2016; Tewari and Parpura 2013). Information transmission between neuron-astrocyte networks plays vital functions in neuronal excitability and plasticity.

In the gray matter, protoplasmic astrocytes, with their sponge-like morphology, establish non-overlapping and exclusive three-dimensional (3D) domain within their neuropilar volume (Bushong et al. 2002, 2004; Rossi 2015). Three-dimensional confocal analysis and electron microscopy showed that protoplasmic astrocytes in rat CA1 stratum radiatum form almost a spherical territory (Bushong et al. 2002; Rossi 2015; Sosunov et al. 2014). In the human brain, the polyhedral domains of protoplasmic astrocytes are arranged repeatedly and uniformly in a 3D

Action Editor: Upinder Singh Bhalla

J. Lorenzo would like to thank the CHED-PhilFrance for the scholarship grant.

Electronic supplementary material The online version of this article (https://doi.org/10.1007/s10827-019-00734-4) contains supplementary material, which is available to authorized users.

✉ Jhunlyn Lorenzo
Jhunlyn_Lorenzo@etu.u-bourgogne.fr

[1] Laboratoire ImViA EA7535, Université de Bourgogne, 9 Avenue Alain Savary, 21078 Dijon, France

[2] DCEE, CEIT, Cavite State University, Indang, Cavite, 4122, Philippines

[3] Department of Integrative and Computational Neuroscience (ICN), Paris-Saclay Institute of Neuroscience (NeuroPSI), CNRS/University Paris-Sud, 1 avenue de la Terrasse, 91198 Gif sur Yvette, France

manner (Robertson 2013). These astrocytes spread radially and create a myriad of leaflet processes during maturation (Bushong et al. 2004; Rossi 2015).

Within a single territory, an astrocyte can influence an average of 4 neurons by enveloping thousands of neuronal structures including the neuronal soma, dendrites, synapse, and axons (Bushong et al. 2002; Debanne and Rama 2011; Halassa et al. 2007; Rossi 2015). According to Debanne and Rama (2011), the spherical volume of an astrocyte in the hippocampus has an approximate diameter of 40 mm, therefore suggesting that it can affect a population of axons. Furthermore, an axon, as it bifurcates, can pass through several astrocytic domains (Robertson 2013). These imply that information transfer is not constrained within the synaptic area but occurs with all cellular elements within the astrocytic domain (Rossi 2015).

Through stimulations on ex vivo systems of CA3 pyramidal neurons of hippocampal slice cultures, Sasaki et al. (2011) investigated the effects Ca^{2+} uncaging of perinodal astrocytes near the unmyelinated axon (150 to 400 μm from the initial segment) on synaptic efficacy. However, physical evidence of direct contact between the node of Ranvier and protoplasmic astrocyte is still lacking. Nonetheless, given that the soma and the unmyelinated axon release glutamate (Glu) and that the expression of astrocytic mGluRs varies, Glu released from these cellular elements may reach astrocytic compartments in proximity (Butt 2011), thus influencing synaptic transmission. Besides, the morphological heterogeneity of astrocyte plays an active role in neuron-astrocyte interaction (Hu et al. 2016). Studies suggest that leaflet processes extend towards the location with high glutamate concentration ([Glu]), predominantly in the synaptic area (Ventura and Harris 1999). Since leaflets are fine processes that are not easily captured by light microscopy (Zhou et al. 2019), it is possible that these processes are not only in contact with synapses but may also contact other neuronal elements where Glu release occurs.

Numerous studies and experiments regarding the role of astrocytes in neuronal activity were already published (De Pittà and Brunel 2016; Manninen et al. 2018). Computational models of biologically-based astrocyte and neuron-astrocyte Ca^{2+} signaling and dynamics, in single cells or networks, have been collected, compared and presented in the literature reviews of Manninen et al. (2018, 2019). However, the gathered models only encompass astrocytes, neuron-astrocyte synapses, and neuron-astrocyte networks, but none regarding nonsynaptic neuron-astrocyte signaling. Astrocyte can sense signals from nonsynaptic neuronal sections because of extrasynaptic transmission, which is the flow of transmitters released from the soma, axon, and dendrites occurring, through exocytosis or spillover, even in the absence of a postsynaptic counterpart (Del-Bel and De-Miguel 2018). For example, localized receptors in the perinodal astrocytic area receive Glu released from the neuronal node of Ranvier (Abbracchio et al. 2009).

Evans and Blackwell (2015) argued that it is time to consider the location of Ca^{2+} influx in computational models aside from the amplitude and duration of intracellular $[Ca^{2+}]$, for the specific site of Ca^{2+} entry also determines the direction of plasticity. Recent physiological studies using higher spatiotemporal resolution revealed compartmentalization in astrocytes dynamics (Volterra et al. 2014). Localized transients $[Ca^{2+}]$ occur more frequently than the transients in the soma (Bazargani and Attwell 2016). In addition, transient Ca^{2+} occurs asynchronously and is functionally independent (Volterra et al. 2014). Dyes experiments in astrocytes revealed that $[Ca^{2+}]$ elevations occur at different spatial and temporal scales in distinct microdomains (Bazargani and Attwell 2016; Sims et al. 2015).

Given these recent discoveries on astrocytes, it is about time to include such astrocytic process to the model of tripartite synapse and synaptic information processing. This study focuses on the molecular exchange that regulates transmission in a closed-loop system comprising the presynaptic neuron, postsynaptic neuron, and astrocyte. Our goal is to present the neuron-astrocyte interaction as biologically plausible as possible. The model presented by Tewari and Majumdar (2012) described the biological processes in detail; with that, we used this as the basis of our study, along with other studies (Chan et al. 2017; Hliatsevich et al. 2015; Mirzakhalili et al. 2018). In their model, the AP originates from the axon initial segment (AIS) and reaches the presynaptic bouton without delay and voltage change. Also, their model focuses on the Ca^{2+} dynamics within the tripartite synapse domain. Hence, we extended their model and incorporated nonsynaptic neuronal and astrocytic elements that may also affect intracellular Ca^{2+} dynamics. Here, the extended model includes compartmentalization of cellular processes, and by doing so, it describes an intercellular relationship rather than a synapse-specific process. The proposed model of the tripartite synapse by Tewari and Majumdar (2012) is therefore modified to include the propagation of AP along the axon, the molecular dynamics in the node of Ranvier for neurotransmitter release, the perinodal astrocytic processes for extrasynaptic signaling, and the compartmentalization of astrocytic Ca^{2+} dynamics via different Ca^{2+} store sites. Biophysical models have been considered to demonstrate the electrical and chemical dynamics on the system and how compartmentalization in astrocytes contributes to information processing and synaptic plasticity. The results suggest that the presence of Ca^{2+} stores positioned on

different astrocytic processes improve the synaptic efficacy by supporting the increase of intracellular astrocytic [Ca^{2+}]. However, the longer the [Ca^{2+}] is above the threshold can create an oversupply of Glu in the extrasynaptic area, which can cause excitotoxic effects.

The remainder of this paper is organized as follows. Section 2 describes the biological characteristics and processes of the neuron-astrocyte model. Section 3 includes the resulting dynamics of a neuron-astrocyte consisting of a synaptic and a perinodal astrocytic area and the investigation on the stochasticity and plasticity of the system using different configurations. Section 4 presents the discussion of the simulation results. Lastly, Section 5 is the conclusion.

2 System model

The tripartite synapse is modeled based on the pyramidal neuron and astrocytes in the hippocampal CA3-CA1 network. Figure 1 illustrates the system morphology, the electrical signals, and the chemical exchanges. The model comprises subsystems indicated by the numbers 1-7, which are further described subsequently. The presynaptic neuron generates AP at the distal end of the AIS (1), then the AP propagates along the myelinated segment (2). The myelin segment attenuates AP; however, when the AP reaches the node of Ranvier (3), it is regenerated, resulting in a higher depolarization and lower hyperpolarization peaks. The pattern of AP attenuation and regeneration continues until it reaches the presynaptic bouton. Calcium dynamics in the node of Ranvier results to the release of neurotransmitters into the perinodal area. The perinodal astrocyte then receives and utilizes the neurotransmitters for intracellular Ca^{2+} release (4). The same Ca^{2+}-dependent neurotransmitter release occurs in the presynaptic bouton, but in this case, the bouton also utilizes the extrasynaptic Glu released by the astrocyte (5). The endoplasmic reticulum in the perinodal and extrasynaptic astrocytic areas process the extracellular Glu. The soma then sums the released intracellular Ca2+ from the compartments, which results in the release of Glu into the extrasynaptic cleft (6). Finally, the membrane potential of the postsynaptic bouton

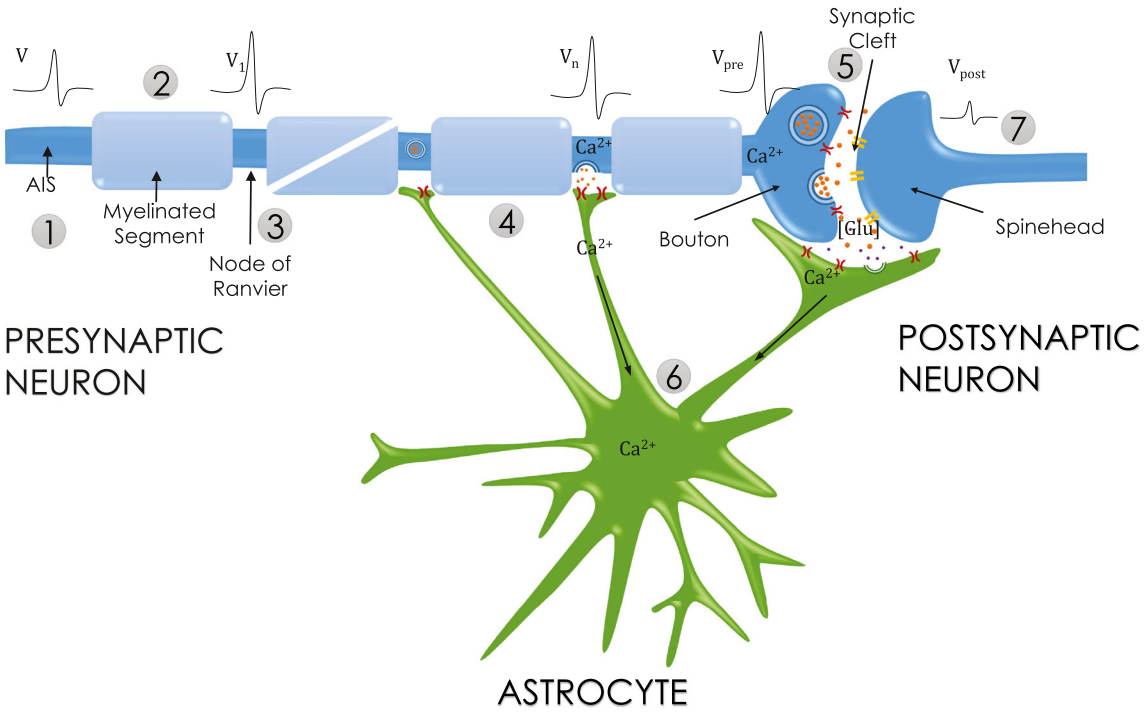

Fig. 1 Tripartite synapse model with perinodal astrocytic components. (1) The AIS generates the AP (V). (2) Then, AP propagates along the myelinated segment and attenuates in the process. (3) In the node of Ranvier, the ionic channels boost AP regeneration and amplification. The saltatory conduction, the process where the magnitude of AP degrades along the myelinated segment and then increases in the node of Ranvier, continues until the AP reaches the presynaptic bouton (axon terminal). (4) The elevations of axonal [Ca^{2+}] result in the molecular transfer of Glu from the unmyelinated axon to the perinodal astrocyte. (5) Neuronal [Ca^{2+}] triggers the release of neurotransmitters into the synaptic cleft and the perinodal area. A portion of the synaptic [Glu] returns to the presynaptic bouton via mGluRs. (6) Transient Ca^{2+} are localized in the astrocyte, compartmentalized in the perinodal area and extrasynaptic area. Astrocytic [Ca2+] activates the release of gliotransmitter into the extrasynaptic area. (7) Postsynaptic spine head receives the synaptic molecules via AMPARs. As a result, the spine head membrane potential (V_{post}) varies with the AMPA current

changes determined by the amount of synaptic Glu (7). The following subsections present a more comprehensive description of each component and their processes.

2.1 Axon initial segment

The AIS, with a length of approximately 10-60 μm (Guo et al. 2017; Nelson and Jenkins 2017), is the neuronal domain separating the axonal and somatodendritic compartments (Yamada and Kuba 2016). It is a critical site where AP is initiated and propagated bidirectionally (to the axon terminals and back to the soma) (Kole and Brette 2018; Nelson and Jenkins 2017; Zbili et al. 2016). Electrical excitability occurs in this site due to the clustering of high-density voltage-gated channels (Kole and Brette 2018; Guo et al. 2017; Nelson and Jenkins 2017), such as voltage-gated Na^+ (Na_v) channels causing the AIS to obtain the lowest AP threshold within the neuron, and voltage-gated K^+ (K_v) channels counteracting the Na_v channels by suppressing AP generation (Yamada and Kuba 2016). Aside from these ionic channels, the location of the AIS plays a vital role in AP generation (Sasaki 2013). It is isolated from the soma, which makes it electrically compact, and its proximal distance from the soma optimizes the charge reaching its domain (Yamada and Kuba 2016). Multi-compartmental studies noted that due to electrotonic isolation, AP generation initiates at the distal end of the AIS (Kole and Brette 2018).

The Hodgkin-Huxley model in Eq. (1) describes the AP generation via the activation and inactivation of ionic channels (Tewari and Majumdar 2012; Sasaki 2013; Li et al. 1650). Here, V (mV) is the membrane potential (in this case, located in the AIS), I_{app} (μA/cm^2) is the applied stimulus, and C (μF/cm^2) is the specific capacitance of the membrane. The potassium, sodium and leak conductances of the ionic channels are given by g_K, g_{Na}, and g_L, with reversal potentials of V_K, V_{Na}, and V_L, respectively. The variable m describes the activation of Na^+ channels while h describes its inactivation. Moreover, n describes the activation of K^+ channels. Table 1 is the list of the parameters used for AP initiation.

$$\begin{aligned}
C\frac{dV}{dt} &= I_{app} - g_K n^4 (V - V_K) - g_{Na} m^3 h (V - V_{Na}) \\
&\quad - g_L (V - V_L), \\
\frac{dx}{dt} &= \alpha_x (1 - x) - \beta_x x, x = m, n, h \\
\alpha_m &= \frac{0.1(-V-45)}{e^{\left(\frac{-V-45}{10}\right)}-1}, \beta_m = 4e^{\left(\frac{-V-70}{18}\right)}, \\
\alpha_h &= 0.07e^{\left(\frac{-V-70}{20}\right)}, \beta_h = \frac{1}{e^{\left(\frac{-V-40}{10}\right)}+1}, \\
\alpha_n &= \frac{0.01(-V-60)}{e^{\left(\frac{-V-60}{10}\right)}-1}, \beta_n = 0.125e^{\left(\frac{-V-70}{80}\right)}.
\end{aligned} \tag{1}$$

2.2 Myelinated segments

The AP, generated at the distal end of the AIS, propagates along the first myelinated segment of the axon. In the central nervous system, the myelin sheaths, formed by oligodendrocytes, wrap the axonal length (Poliak and Peles 2003; Freeman et al. 2016). Electrically, these sheaths have significant resistance and low capacitance. Furthermore, the ionic channel density along the myelinated segment is low, causing a passive voltage spread (Bucher and Goaillard 2011).

The cable equation, given in Eq. (2), describes the myelinated segment of the axon as a transmission line consisting of resistive and capacitive properties (Bogatov et al. 2014).

$$\frac{r}{2\rho_a}\frac{\partial^2 v}{\partial x^2} - C\frac{\partial v}{\partial t} - \frac{v}{\rho_m l} + \frac{G(v)}{2\pi r} = 0, \tag{2}$$

where v is the difference between the membrane potential and the resting potential (Woo and Choi 2007), r is the radius of the axon, ρ_a is the axoplasmic resistivity, ρ_m is the membrane resistivity, and l is the membrane thickness. The charge generation function $G(v)$ determines the ionic exchanges within the segment, and it is equal to $\beta \cdot v$ where β is the generation constant with values ranging from 0 to any

Table 1 Action potential initiation along the axon initial segment

Parameter	Value	Description
C	1	Specific capacitance of the membrane, μF/cm^2
g_K	36	K^+ channel conductance, mS/cm^2
g_{Na}	120	Na^+ channel conductance, mS/cm^2
g_L	0.3	Leak conductance, mS/cm^2
V_K	–82	K^+ channel reversal potential, mV
V_{Na}	45	Na^+ channel reversal potential, mV
V_L	–59.4	Leak reversal potential, mV

Table 2 AP propagation along the myelinated segments

Parameter	Value	Description
r	0.5	Radius of the myelinated axon, μm (Gulledge and Bravo 2016)
l	1	Thickness of the myelin sheath, μm (Gulledge and Bravo 2016)
x_m	100	Length of the myelin segment, μm (Gulledge and Bravo 2016)
n_m	20	Number of myelin segments (Gulledge and Bravo 2016)
C_m	0.1	Membrane capacitance of the myelin segment, μF/cm^2 (Gulledge and Bravo 2016)
ρ_m	10^7	Membrane resistivity, Ω-m (of Notre Dame 2004)
ρ_a	1.1	Axoplasmic resistivity, Ω·m (of Notre Dame 2004)
β	0	Generation constant (Bogatov et al. 2014)

positive real number (Bogatov et al. 2014). Bogatov et al. (2014) presented the approximate solution in Eq. (3) of the cable equation and showed the relationship of the AP with the distance traveled, x, from the point of initiation and the propagation time t.

$$v(x,t) \approx e^{-\frac{x\sqrt{\gamma}}{\lambda}} v_0 \left(t - \frac{\tau x}{2\lambda\sqrt{\gamma}} \right) \tag{3}$$

Three constant parameters were produced: λ (in mm) is the length constant which determines the maximum distance the AP can travel without considerate attenuation, τ in (ms) is the time constant which is the maximum propagation time before the signal decay, and γ (from 0 to 1) is the constant of distributed AP that describes the ionic exchanges within the segment. These parameters are

$$\lambda = \sqrt{\frac{rl\rho_m}{2\rho_a}}, \tau = l\rho_m C, \gamma = 1 - \frac{\beta l \rho_m}{2\pi r}.$$

The AP propagation within the myelinated segments uses this approximation. Because of the small capacitance and considerable resistance of the myelin (Poliak and Peles 2003), the length constant of the axonal cable is longer while its time constant is shorter than in unmyelinated segments (Bucher and Goaillard 2011).

The current density at the end of the myelinated segment serves as the stimulus that regenerates the AP generation at the node of Ranvier. Electrophysiological studies showed that the node of Ranvier follows the spike frequency of the AP initiated in the AIS with ∼100 μs delay (Kole 2011). The current density I_n flowing into the node is computed as the change in voltage over time (of Notre Dame 2004) so that $I_n = CdV_m/dt$ where V_m is the voltage at the point in the axon where the myelin segment ends. Table 2 shows the parameters involved in the calculation of membrane potential in the myelinated segment.

2.3 Node of Ranvier

The section between the myelin segments is called the node of Ranvier, with a nodal length of approximately 0.3 to 1.4 μm (Babbs and Shi 2013; Arancibia-Carcamo et al. 2017). Arancibia-Carcamo et al. (2017) measured the node lengths of the myelinated axons. As a result, they found that the nodal length is consistent along an axon, but differs between axons. The node length and the number of Na_v channels in the node has a positive correlation indicating a constant channel density. The densities of transmembrane inactivating Na^+ and low-threshold K^+ channels are also much higher in the node of Ranvier than in the soma and in the AIS (Ye and Ng 2018; Babbs and Shi 2013; Ford et al. 2015). Therefore, there is a lower threshold of AP activation in this compartment (Ye and Ng 2018). The AP regeneration

Table 3 AP propagation in the node of Ranvier

Parameter	Value	Description
g_{Na_n}	266.7	Nodal Na^+ channel conductance, mS/cm^2 (Gulledge and Bravo 2016)
g_{K_n}	66.7	Nodal K^+ channel conductance, mS/cm^2 (Gulledge and Bravo 2016)
g_{L_n}	1.76	Nodal leak conductance, mS/cm^2 (Ford et al. 2015)
V_{Na_n}	55	Nodal Na^+ channel reversal potential, mV (Ford et al. 2015)
V_{K_n}	–90	Nodal K^+ channel reversal potential, mV (Ford et al. 2015)
V_{L_n}	–70	Nodal leak reversal potential, mV (Gulledge and Bravo 2016)

in these compartments also follows the Hodgkin-Huxley model in Eq. (1) using channel conductance and reversal potentials specific in the node. (Refer to Table 3).

The periodic interval between myelin segments and nodes of Ranvier causes the AP to propagate in a "saltatory" or jumping manner that speeds up the AP propagation (Babbs and Shi 2013). In saltatory conduction, the AP amplitude, initiated in the AIS, diminishes as it propagates along the myelinated segment, and intensifies at the node. This activity repeatedly occurs until the AP reaches the axon terminals. The voltage-gated mechanisms in the nodes enable the regulation of AP waveform (Kole 2011).

2.4 Perinodal area

We considered the node of Ranvier and perinodal astrocyte as compartments due to their properties similar to the synapse. For the following specific reasons, we have taken the perinodal area into account. First is the presence of vesicles containing neurotransmitters in the nodes. These vesicles are packaged in the soma, then are transported into the axon terminals and captured by axonal varicosities. Uncaptured vesicles leave the terminal and re-enter circulation (Kuznetsov and Kuznetsov 2017). Second, in the central nervous system, the nodes are connected

Table 4 Presynaptic neuron calcium dynamics[a]

Parameter	Value	Description
A	1.2398×10^{-8}	Surface area of the bouton or
	1.9735×10^{-8}	the node cm^2 (Gulledge and Bravo 2016)
v_c	1.29818×10^{-16}	Volume of the bouton or
	3.0995×10^{-16}	the node, L (Gulledge and Bravo 2016)
z_{Ca}	2	Calcium valence
F	96487	Faraday's constant, C/mole
ρ_{Ca}	3.2	N-type channel density, μm^{-2}
g_{Ca}	2.3	N-type channel conductance, pS
V_{Ca}	125	Ca^{2+} reversal potential, mV
R	8.314	Real gas constant, J/K
T	293.15	Absolute temperature, K
c_{ext}	2	External Ca^{2+} concentration, mM
c_i^{rest}	0.1	Resting intracellular [Ca^{2+}], μM
$\tau_{m_{Ca}}$	10	Time constant, ms
$V_{m_{Ca}}$	–17	Half-activation voltage of N-type Ca^{2+}
		channel, mV
$k_{m_{Ca}}$	8.4	Slope factor of N-type Ca^{2+} channel, mV
i_{PMCa}	0.4	Maximum PMCa current, $\mu A/cm^2$
K_{PMCa}	0.1	[Ca^{2+}] at which v_{PMCa} is halved, μM
v_{leak}	0.001022	Maximum leak of Ca^{2+}, ms^{-1}
a_2	0.2	Inhibitory Ca^{2+} binding constant, μM/s
c_1	0.1850	Ratio of the ER volume to the volume of the bouton and volume of the node
v_1	30	Maximum IP_3 receptor flux, s^{-1}
v_2	0.2374	Ca^{2+} leak rate constant, μs^{-1}
v_3	0.9	SERCA maximal pump rate, μM/s
k_3	0.1	SERCA dissociation constant, μM
d_1	0.13	IP_3 dissociation constant, μM
d_2	1.049	Inhibitory Ca^{2+} dissociation constant, μM
d_3	943.4	IP_3 dissociation constant, nM
d_5	82.34	Activation Ca^{2+} dissociation constant, nM
v_g	0.062	Maximum production rate of IP_3, μM/s
k_g	0.78	Glutamate concentration at which v_g is halved, nM
τ_p	0.14	IP_3 degradation constant, s^{-1}
p_0	160	Initial IP_3 concentration, nM

[a]Unless otherwise stated, the parameter values are from the study of Tewari and Majumdar (2012) and Chan et al. (2017)

Table 5 Neurotransmitter release[a]

Parameter	Value	Description
α	0.3	Ca^{2+} association rate constant, μM/ms
β	3	Ca^{2+} dissociation rate constant , per ms
γ	30	Forward isomerization rate constant, per ms
Δ	8	Backward isomerization rate constant, per ms
τ_{rec}	800	Vesicle recovery time constant, ms
τ_{inact}	3	Vesicle inactivation time constant, ms
a_1	50	$[Ca^{2+}]$ at which λ is halved, μM
a_2	5	Slope factor of spontaneous release rate λ, μM
a_3	0.85	Maximum spontaneous release rate, per ms
n_v	2	Number of docked vesicles in the bouton
n_v	1	Number of docked vesicles in the node
g_v	60	Glutamate concentration in a single vesicle, mM
g_c	10	Glutamate clearance rate constant, per ms

[a]The parameter values are from the study of Tewari and Majumdar (2012)

to perinodal astrocytes (Poliak and Peles 2003; Dutta et al. 2018) which occupy the space between myelinated segments in the axon and show biochemical characteristics when connected. AP influences the release of Glu from the unmyelinated section of the axon. This release is dependent on the $[Ca^{2+}]$ elevation attributable to AP and endoplasmic reticulum (ER) extending throughout the axon (de Juan-Sanz et al. 2017; Genç et al. 2017). This nonsynaptic neurotransmitter release (Ziskin et al. 2007) influences the opening of Glu receptors in the perinodal astrocyte

Table 6 Astrocyte dynamics parameters[a]

Parameter	Value	Description
r_{c_a}	6	Maximal IP_3R flux, per s
r_L	0.11	Maximal rate of Ca^{2+} from ER, per s
c_0	2	Total cell free $[Ca^{2+}]$, μM
$c_{1,a}$	0.185	Ratio of ER volume to cytosol volume
v_{ER}	0.9	Maximal rate of SERCA uptake, μM/s
K_{ER}	0.1	SERCA Ca^{2+} affinity, μM
d_1	0.13	IP_3 dissociation constant, μM
d_2	1.049	Ca^{2+} inactivation dissociation constant, μM
d_3	0.9434	IP_3 dissociation constant, μM
d_5	0.08234	Ca2+ activation dissociation constant, μM
a_2	2	IP_3R binding rate for Ca^{2+} inhibition, per s
N	20	Number of IP_3Rs in a cluster
v_β	0.5	Maximal rate of IP_3 production by PLCβ, μM/s
K_R	1.3	Glutamate affinity of the receptor, μM
K_P	10	Ca^{2+}/PKC-dependent inhibition factor, μM
K_π	0.6	Ca^{2+} affinity of PKC, μM
v_δ	0.05	Maximal rate of IP_3 production by PLCδ, μM/s
$K_{PLC\delta}$	0.1	Ca^{2+} affinity of PLCδ, μM
k_δ	1.5	Inhibition constant of PLCδ activity, μM
r_{5pa}	0.05	Maximal rate of degradation by IP-5P, per s
v_{3K}	2	Maximal rate of degradation by IP_3-3K, μM/s
K_D	0.7	Ca^{2+} affinity of IP_3-3K, μM
K_3	1	IP_3 affinity of IP_3-3K, μM

[a]The parameter values are from the study of Tewari and Majumdar (2012)

(Abbracchio et al. 2009). Lastly, while communication is classically known to occur at synapses, evidence shows that extrasynaptic transmitter release, from the soma, axon, and dendrites occurs even in the absence of a postsynaptic counterpart, via exocytosis or spillover (Del-Bel and De-Miguel 2018; De Pittà et al. 2016; Trueta and De-Miguel 2012). The Ca^{2+} dynamics and Glu dynamics on the node, perinodal area, and perinodal astrocyte follow the models presented in Sections 2.5 and 2.6. Biophysical properties and parameters related to the perinodal section are in Tables 4, 5, 6 and 7.

2.5 Presynaptic bouton

The AP generation in the AIS, nodes of Ranvier, and the axon terminal leads to a local increase in cytosolic $[Ca^{2+}]$ (Tewari and Majumdar 2012). The change in $[Ca^{2+}]$ in a compartment is attributed to the fast kinetics of AP and the intracellular molecular events generating Ca^{2+} (Tewari and Majumdar 2012; Mirzakhalili et al. 2018). Here, the total $[Ca^{2+}]$ in the compartment, c_i is equal to the summation of the $[Ca^{2+}]$ due to AP, c_{fast}, and the intracellular transient $[Ca^{2+}]$, c_{slow} as described by

$$c_i = c_{fast} + c_{slow}. \tag{4}$$

2.5.1 Fast calcium dynamics

The fast Ca^{2+} dynamics, through voltage-dependent calcium channels (VDCC) (Hliatsevich et al. 2015), is governed by the construction-destruction formula (Tewari and Majumdar 2012)

$$\frac{dc_{fast}}{dt} = -\frac{I_{Ca}A}{z_{Ca}Fv_c} + J_{PMleak} - \frac{I_{PMCa}A}{z_{Ca}Fv_c}. \tag{5}$$

Here, I_{Ca} is the current in the N-type Ca^{2+} channel, A is the surface area of the compartment, z_{Ca} is the Ca^{2+} ion valence, F is the Faraday's constant, and v_c is the volume of the compartment.

In the equation of the current surface density through the N-type VDCC in Eq. (6), ρ_{Ca} is the N-type channel surface density, g_{Ca} is the single N-type Ca^{2+} conductance (Tewari and Majumdar 2012; Hliatsevich et al. 2015).

$$I_{Ca} = \rho_{Ca} m_{Ca}^2 g_{Ca} \left(V - V_{Ca}\right), \tag{6}$$

The Nernst equation in Eq. (7) determines the Ca^{2+} reversal potential, where R is the real gas constant, T is the absolute temperature, c_{ext} is the extracellular $[Ca^{2+}]$ and c_i^{rest} is the total intracellular Ca^{2+} at rest (Tewari and Majumdar 2012; Hliatsevich et al. 2015).

$$V_{Ca} = \frac{RT}{z_{Ca}F} \ln\left(\frac{c_{ext}}{c_i^{rest}}\right), \tag{7}$$

The variable m_{Ca} is the opening probability of a single gate in a two-gate N-type Ca^{2+} channel which is only open when the two gates are both open (Tewari and Majumdar 2012). The probability is time-dependent, so that

$$\frac{dm_{Ca}}{dt} = \frac{\left(m_{Ca}^{\infty} - m_{Ca}\right)}{\tau_{m_{Ca}}}. \tag{8}$$

The Boltzmann-function in Eq. (9) approximates the dependence of m_{Ca}^{∞} on the membrane potential fitted to the whole-cell current of an N-type Ca^{2+} channel. $\tau_{m_{Ca}}$ is the time constant when m_{Ca} approaches its asymptotic value and m_{Ca}^{∞} (Tewari and Majumdar 2012; Hliatsevich et al. 2015).

$$m_{Ca}^{\infty} = \frac{1}{1 + exp\left(\left(V_{m_{Ca}} - V\right)/k_{m_{Ca}}\right)}. \tag{9}$$

Table 7 Astrocytic gliotransmitter release[a]

Parameter	Value	Description
k_1^+	3.75×10^{-3}	Ca^{2+} association rate for site S_1, per μMms
k_1^-	4×10^{-4}	Ca^{2+} dissociation rate for site S_1, per ms
k_2^+	2.5×10^{-3}	Ca^{2+} association rate for site S_2, per μMms
k_2^-	1×10^{-3}	Ca^{2+} dissociation rate for site S_2, per ms
k_3^+	1.25×10^{-2}	Ca^{2+} association rate for site S_3, per μMms
k_3^-	10×10^{-3}	Ca^{2+} dissociation rate for site S_3, per ms
$\tau_{rec,a}$	800	Vesicle recovery time constant, ms
$\tau_{inact,a}$	3	Vesicle inactivation time constant, ms
$c_{thresh,a}$	196.69	Astrocyte response threshold, nM
$n_{v,a}$	12	Number of SLMV ready to be released
$g_{v,a}$	20	[Glu] in each vesicle, mM
$g_{c,a}$	10	Glutamate clearance rate, per ms

[a]The parameter values are from the study of Tewari and Majumdar (2012)

I_{PMCa} is the current due to Ca^{2+} ATPase given by the expression

$$I_{PMCa} = i_{PMCa} \frac{c_i^2}{c_i^2 + K_{PMCa}^2}, \tag{10}$$

where v_{PMCa} is the maximum PMCa current and K_{PMCa} is the $[Ca^{2+}]$ at half of v_{PMCa}. Then, J_{PMleak} in Eq. (11) is the leak from the extracellular space into the compartment and is added to ensure that the $[Ca^{2+}]$ will not decrease to 0.

$$J_{PMleak} = v_{leak} \left(c_{ext} - c_i\right). \tag{11}$$

Here, v_{leak} is the maximal $[Ca^{2+}]$ and c_{ext} is the external $[Ca^{2+}]$ (Tewari and Majumdar 2012).

2.5.2 Slow calcium dynamics

The slow Ca^{2+} dynamics, c_{slow}, is attributed to the release of Ca^{2+} from the ER triggered by the production of inositol-triphosphate (IP_3) (Tewari and Majumdar 2012; Chan et al. 2017; Ding et al. 2018). The binding of the Glu (from astrocytic release) and the Glu receptors in the neuronal membrane produce IP_3 (Tewari and Majumdar 2012). This intracellular messenger then binds with IP_3 receptors to trigger the ER release of Ca^{2+} (Ding et al. 2018). The ER membrane also has ATPase (Sarco-Endoplasmic Reticulum ATPase (SERCA) pump) that pumps Ca^{2+} into the depot (Hliatsevich et al. 2015). The Li-Rinzel model describes the dynamical system governing the cslow behavior (Tewari and Majumdar 2012; Chan et al. 2017; Ding et al. 2018; Hliatsevich et al. 2015; Wade et al. 2011) given as

$$\frac{dc_{slow}}{dt} = -J_{chan} - J_{ERpump} - J_{ERleak}, \tag{12}$$

where J_{chan} is the Ca^{2+} flowing out of the ER into the intracellular space via IP_3 release channels, J_{ERpump} is the Ca^{2+} flowing into the ER from the cytosol caused by the SERCA pump (Hliatsevich et al. 2015), and J_{ERleak} is the Ca^{2+} ions leaking from the ER into the cytosol.

$$\begin{aligned}
J_{chan} &= c_1 v_1 m_\infty^3 n_\infty^3 q^3 \left(c_i - c_{ER}\right), \\
\frac{dp}{dt} &= v_g \frac{g_a^{0.3}}{k_g^{0.3} + g_a^{0.3}} - \tau_p \left(p - p_0\right), \\
\frac{dq}{dt} &= \alpha_q \left(1 - q\right) - \beta_q q, \\
m_\infty &= \frac{p}{p + d_1}, n_\infty = \frac{c_i}{c_i + d_5}, \\
\alpha_q &= a_2 d_2 \frac{p + d_1}{p + d_3}, \beta_q = a_2 c_i, \\
\frac{dc_{ER}}{dt} &= -\frac{1}{c_1} \frac{dc_{slow}}{dt}.
\end{aligned} \tag{13}$$

In this Ca^{2+} flux, c_1 is the ratio of the ER volume and the compartment volume, p is the intracellular IP_3 concentration, g_a is the extracellular [Glu] (e.g., released by the astrocyte), q is the fraction of activated IP_3, and c_{ER} is the $[Ca^{2+}]$ in the ER. Then, the remaining fluxes are given in Eqs. (14) and (15).

$$J_{ERpump} = \frac{v_3 c_i^2}{k_3^2 + c_i^2} \tag{14}$$

$$J_{ERleak} = c_1 v_2 \left(c_i - c_{ER}\right) \tag{15}$$

Refer to Table 4 for the parameters of the compartments.

There are two conditions for neurotransmitters release from the node and presynaptic compartment. First, Glu is released when five Ca^{2+} ions bind to the Ca^{2+} sensor of the vesicle (Tewari and Majumdar 2012). The arrival of AP evokes the release, and with correlation with the intracellular $[Ca^{2+}]$ (Tewari and Majumdar 2012; De Pittà and Brunel 2016). Second, the intracellular $[Ca^{2+}]$ can also randomly provoke vesicles to release neurotransmitters. Whether evoked or spontaneous, the vesicle release process is inactive 6.34 ms after release (Tewari and Majumdar 2012).

Five Ca^{2+} ions must bind with the Ca^{2+} sensor. The kinetic model

$$X \underset{\beta}{\overset{5\alpha c_i}{\rightleftarrows}} X(c_i)_1 \underset{2\beta}{\overset{4\alpha c_i}{\rightleftarrows}} X(c_i)_2 \underset{3\beta}{\overset{3\alpha c_i}{\rightleftarrows}} X(c_i)_3 \underset{4\beta}{\overset{2\alpha c_i}{\rightleftarrows}} X(c_i)_4 \underset{5\beta}{\overset{\alpha c_i}{\rightleftarrows}} X(c_i)_5 \underset{\delta}{\overset{\gamma}{\rightleftarrows}} X(c_i)_5^* \tag{16}$$

describes the binding process, where α and β are the Ca^{2+} association and dissociation rate constants, and γ and δ are the Ca^{2+} independent isomerization constants. Here, X is the Ca^{2+} sensor with no Ca^{2+}, $X(c_i)_1$ is the Ca^{2+} sensor with one Ca^{2+} bound, $X(c_i)_2$ has two Ca^{2+}, until $X(c_i)_5^*$ which is the isomer of $X(c_i)_5$ ready for Glu release. The transition of the Ca^{2+} sensor from one state to another is computed using Markov model for ionic channels. Following the study of Tewari and Majumdar (2012), two docked vesicles are present in the bouton. Therefore, f_r, (with values 0, 0.5, and 1) represents the fraction of the ready vesicles out of the total number of docked vesicles in the bouton. Voltage-dependent Ca^{2+} channels open with the arrival of AP, consequently increasing $[Ca^{2+}]$, thus promoting vesicle release (De Pittà and Brunel 2016).

Furthermore, based on the amount of intracellular $[Ca^{2+}]$, the spontaneous vesicle release is also possible even in the absence of AP. In the study of Modchang et al. (2010) comparing stochastic and deterministic approaches on vesicle release, the result suggested that in synapses with nanodomain, stochastic vesicle release algorithm is more accurate than deterministic approach. Because this is a stochastic process, the Poisson random number determines the number of docked vesicles ready for release, with the mean parameter given by

$$\lambda(c_i) = a_3 \left(1 + exp\left(\frac{a_1 - c_i}{a_2}\right)\right). \tag{17}$$

Vesicles undergo a fusion and recycling process governed by Eq. (18). Here, R is the fraction of releasable vesicles in the compartment, E is the fraction of effective vesicles in the synaptic or extrasynaptic cleft, and I is the fraction of vesicles undergoing recycling. The time constant τ_{inact} and τ_{rec} are for the vesicle inactivation and recovery time (Tewari and Majumdar 2012). The synaptic release is history-depen-dent, therefore, if the next incoming AP is in the order of these time constants, vesicles are neither replenished nor released (De Pittà and Brunel 2016).

$$\begin{aligned} \frac{dR}{dt} &= \frac{1}{\tau_{rec}} - f_r R, \\ \frac{dE}{dt} &= -\frac{E}{\tau_{inact}} + f_r R, \\ I &= 1 - R - E. \end{aligned} \tag{18}$$

Equation (19) describes the Glu dynamics explicitly in the CA3-CA1 synapse. Here, g is the Glu concentration in the cleft, n_v is the number of docked vesicles in the compartment, g_v is the Glu concentration inside a vesicle, and g_c is the rate of Glu clearance caused by the diffusion from the cleft and the reversal uptake of neuron or astrocyte (Tewari and Majumdar 2012; Chan et al. 2017). Table 5 presents the parameters in this process.

$$\frac{dg}{dt} = n_v g_v E - g_c g \tag{19}$$

2.6 Astrocyte

Astrocytes are the most abundant cell (glial cells) in the brain, which surround synapses, sense neuronal activity, and influence information processing (Perea et al. 2014; Sims et al. 2015; Nazari et al. 2015). Astrocytes also have channels such as K^+, $Na^+$and Ca^{2+}, just like in neurons. However, the dominance of K^+ channels hinders the astrocyte from generating APs. Therefore, it is agreed that Ca^{2+} is the principal signaling mechanism of astrocytes as it shows intrinsic excitability via changes in intracellular [Ca^{2+}] (Manninen et al. 2018; Perea et al. 2014). Transient [Ca^{2+}] increases in response to synaptic activity (Volterra et al. 2014) and propagates within the astrocyte, into the soma, or nearby cells (Bazargani and Attwell 2016). The discovery of this Ca^{2+} wave suggests that astrocytes integrate and transfer signals (Heller and Rusakov 2017). In this model, the extrasynaptic astrocyte and the perinodal astrocyte are different compartments whose Ca^{2+} transients flow into the soma for integration and vesicle packaging. In the astrocyte, Ca^{2+} oscillation is attributed to the Ca^{2+}-induced Ca^{2+} release (CICR) from the ER into the cytosol through IP_3 receptors (Ashhad and Narayanan 2018; Kelso et al. 2013; Wallach et al. 2014). ER in the astrocytes forms an extended network of tubes and vesicles through the cytoplasm via plasma membrane contact (Ashhad and Narayanan 2018; Kelso et al. 2013).

Astrocyte responds to synaptic activity by changes in its global (somatic) and focal (perisynaptic and perinodal) Ca^{2+} elevations (Guerra-Gomes et al. 2018; Volterra et al. 2014). Intracellular [Ca^{2+}] transients can propagate along the process and into the soma, which may influence somatic [Ca^{2+}] elevations (Bazargani and Attwell 2016; Gordleeva et al. 2018). Subsequently, the overall summation of somatic and transient [Ca^{2+}] leads to transmitter release (Cinciute 2019). However, biophysical mechanisms of astrocytic Ca^{2+} intracellular propagation is still insufficient (Gordleeva et al. 2018), specifically if global [Ca^{2+}] elevations result from the linear summation of transient Ca^{2+} (Guerra-Gomes et al. 2018). Here, we, therefore, assumed that the total intracellular [Ca^{2+}] is responsible for astrocytic vesicle release. Astrocyte dynamics is a stochastic process, and the total intracellular [Ca^{2+}] is the summation of all the transient Ca^{2+}. Equation (20) describes the intracellular Ca^{2+} dynamics.

$$\begin{aligned} &\frac{dc_a}{dt} = J_{chan,a} - J_{pump,a} + J_{leak,a}, \\ &J_{chan,a} = \left(r_{c_a} m_{\infty,a}^3 n_{\infty,a}^3 h_a^3\right)\left(c_0 - \left(1 + c_{1,a}\right) c_a\right), \\ &J_{pump,a} = v_{ER} \frac{c_a^2}{c_a^2 + K_{ER}^2}, \\ &J_{leak,a} = r_L \left(c_0 - \left(1 + c_{1,a}\right) c_a\right). \end{aligned} \tag{20}$$

Here, $J_{chan,a}$ is the Ca^{2+} flux flowing out of the ER into the intracellular space, where r_{c_a} is the maximal rate of the Ca^{2+} flux from the IP_3R clusters while the product $m_\infty^3 n_\infty^3 h_a^3$ is the opening probability of the IP_3 cluster. $J_{pump,a}$ is the rate at which Ca^{2+} is removed from the intracellular space by SERCA pump, where v_{ER} is the maximal rate of Ca^{2+} uptake into the ER and K_{ER} is the intracellular Ca^{2+} affinity of the pump. Moreover, $J_{leak,a}$ is the Ca^{2+} leaking from the ER into the intracellular space where r_L is the maximal rate of Ca^{2+} leak from the ER. The Ca^{2+} dynamics is almost similar to the dynamics of c_{slow}. It is based on a closed-cell in which the $[Ca^{2+}]_{ER,a}$ is given by $c_{ER,a} = (c_0 - c_a)/c_{1,a}$. In $J_{chan,a}$, r_{c_a} is the maximal rate of the Ca^{2+} flux from the IP_3R clusters while the product $m_{\infty,a}^3 n_{\infty,a}^3 h_a^3$ is the opening probability of the IP_3 cluster (Tewari and Majumdar 2012; Li et al. 1650).

Information transfer from one neuron to an astrocyte occurs through the spillover of transmitters (Volterra et al. 2014; Li et al. 1650). High-affinity G protein-coupled receptors in the astrocytic membrane receive neurotransmitters that trigger the production of IP_3. The IP_3 production given in Eq. (21) includes a mass balance of agonist-dependent and agonist-independent production (first two terms on the right-hand side) and IP_3 degradation

by IP_3 -3K and IP-5P respectively (Tewari and Majumdar 2012; De Pittà and Brunel 2016; Li et al. 1650).

$$\begin{aligned}\frac{dp_a}{dt} = & v_\beta \text{Hill}\left(g^{0.7}, K_R\left(1+\frac{K_p}{K_R}\text{Hill}\left(C, K_\pi\right)\right)\right)\\ & +\frac{v_\delta}{1+\frac{p_a}{k_\delta}}\text{Hill}\left(c_a^2, K_{PLC\delta}\right)\\ & -v_{3K}\text{Hill}\left(c_a^4, K_D\right)\text{Hill}\left(p_a, K_3\right)-r_{5p_a}p_a.\end{aligned} \tag{21}$$

The remaining parameters are as follows.

$$\begin{aligned}\text{Hill}(x^n, K) &= \frac{x^n}{x^n+K^n},\\ m_{\infty,a} &= \text{Hill}(p_a, d_1),\\ n_{\infty,a} &= \text{Hill}(c_a, d_5),\\ \alpha_{h_a} &= a_2 d_2 \frac{p_a+d_1}{p_a+d_3},\\ \beta_{h_a} &= a_2 c_a,\\ \frac{dh_a}{dt} &= \alpha_{h_a}(1-h_a)-\beta_{h_a}h_a+G_h(t).\end{aligned}$$

The parameters α_{h_a} and β_{h_a} are the rates at which h_a opens and closes, respectively. $G_h(t)$ is a zero-mean, uncorrelated, Gaussian white noise with covariance (Tewari and Majumdar 2012) in

$$\left\langle G_h(t)G_h(t')\right\rangle = \frac{\alpha_{h_a}(1-h_a)+\beta_{h_a}h_a}{N_{IP_3}}\delta(t-t'), \tag{22}$$

The values of the parameters are presented in Table 6.

The endoplasmic reticulum releases IP_3-dependent Ca^{2+} (Volterra et al. 2014). As a consequence, the intracellular increase of $[Ca^{2+}]$ induces the release of gliotransmitters, such as Glu (Volterra et al. 2014; Li et al. 1650). Researches detected vesicle type structures or synaptic-like microvesicles (SLMVs) in astrocyte (Bezzi and Volterra 2014; Jourdain et al. 2007; Volterra and Meldolesi 2005), concluding that gliotransmitters are released using the same mechanism in neurons, and are Ca^{2+}-dependent as well (De Pittà et al. 2016). In the study of Tewari and Majumdar (2012), three Ca^{2+} ions must bind with three independent gates (S_1, S_2, and S_3) for possible gliotransmitter release following the kinetic model

$$C_a + C_j \underset{k_j^-}{\overset{k_j^+}{\rightleftarrows}} O_j,\ j=1,2,3. \tag{23}$$

The gate S_j opens and closes according to O_j and C_j probabilities, respectively, with the opening and closing rates of k_j^+ and k_j^-, respectively. The open gate O_j has a temporal evolution of

$$\frac{dO_j}{dt} = k_j^+ c_a - (k_j^+ c_a + k_j^-)O_j. \tag{24}$$

The product of the opening probabilities of the three sites in Eq. (25) gives the fraction of the SLMVs ready for release.

$$f_r^a = O_1 \cdot O_2 \cdot O_3 \tag{25}$$

Astrocytic vesicle fusion and recycling uses an almost similar transmitter release process as the presynaptic neuron, described as

$$\begin{aligned}\frac{dR_a}{dt} &= \frac{I_a}{\tau_{rec,a}} - \Theta\left(c_a - c_{thresh,a}\right) f_r^a R_a,\\ \frac{dE_a}{dt} &= -\frac{E_a}{\tau_{inact,a}} + \Theta\left(c_a - c_{thresh,a}\right) f_r^a R_a,\\ I_a &= 1 - R_a - E_a,\end{aligned} \tag{26}$$

where R_a is the fraction of SLMVs inside the astrocyte ready for release, E_a is the fraction of SLMVs in the cleft, and I_a is the faction of SLMVs undergoing re-acidification. The symbol Θ is the Heaviside function, and $c_{thresh,a}$ is the amount of $[Ca^{2+}]$ needed to activate the release site. The time constants $\tau_{inact,a}$ and $\tau_{rec,a}$ are for the inactivation and recovery of SLMVs, respectively. Gliotransmitters are released if the intracellular $[Ca^{2+}]$ is beyond the threshold (De Pittà and Brunel 2016).

The Glu released by the astrocyte is necessary for presynaptic IP_3 production. Its dynamics is modeled as

$$\frac{dg_a}{dt} = n_{v,a}g_{v,a}E_a - g_{c,a}g_a. \tag{27}$$

Here, g_a is the [Glu] in the cleft, $n_{v,a}$ is the number of releasable SLMVs ready for release, $g_{c,a}$ is the [Glu] inside a vesicle, and $g_{ca,a}$ is the clearance rate of Glu from the cleft (Tewari and Majumdar 2012). Refer to Table 7 for the parameters.

2.7 Postsynaptic spinehead

Synaptic Glu then activates postsynaptic firing (Li et al. 1650). In the dendritic spine, α-amino-3-hydroxy-5-methyl-4-isoxazoleproprionic acid receptors (AMPARs) are clustered and localized at glutamatergic synapses (Tewari and Majumdar 2012). The postsynaptic membrane potential, as shown in Eq. (28), develops in the passive postsynaptic membrane.

$$\tau_{post}\frac{dV_{post}}{dt} = -\left(V_{post} - V_{post}^{rest}\right) - R_m I_{AMPA}, \tag{28}$$

where V_{post} is the postsynaptic membrane potential, V_{post}^{rest} is the postsynaptic resting membrane potential, R_m is the spine resistance, and I_{AMPA} is the AMPAR current computed as

$$I_{AMPA} = g_{AMPA}m_{AMPA}\left(V_{post} - V_{AMPA}\right). \tag{29}$$

Here g_{AMPA} is the AMPAR channel conductance, and m_{AMPA} is the AMPAR gating variable. The gating variable follows the Hodgkin-Huxley type formulism

$$\frac{dm_{AMPA}}{dt} = \alpha_{AMPA}g\left(1-m_{AMPA}\right) - \beta_{AMPA}m_{AMPA}, \tag{30}$$

Table 8 Postsynaptic neuron membrane potential[a]

Parameter	Value	Description
R_m	0.79×10^5	Spine-head resistance, MΩ
V_{post}^{rest}	–70	Postsynaptic resting membrane potential, mV
τ_{post}	50	Postsynaptic membrane time constant, ms
g_{AMPA}	0.35	AMPAR conductance, nS
V_{AMPA}	0	AMPAR reversal potential, mV
α_{AMPA}	1.1	AMPAR forward rate constant, μM/ms
β_{AMPA}	190	AMPAR backward rate constant, per s

[a]The parameter values are from the study of Tewari and Majumdar (2012)

where α_{AMPA} and β_{AMPA} are the opening and closing rate of the receptor, respectively, and g is the [Glu] in the cleft. Refer to Table 8 for the list of parameters and their corresponding values.

3 Simulation results

The dynamics were simulated in Matlab, using the Euler method, with a timestep of $\Delta t = 0.05$ ms. In this model, there are 20 myelinated segments in the presynaptic axon (Gulledge and Bravo 2016), forming 41 compartments: one AIS, 20 myelinated segments, 19 nodes of Ranvier, and one presynaptic bouton. The AIS input is a pulse wave of μA/cm^2 with a frequency of 5 Hz and a pulse width of 4 ms (Wallach et al. 2014; Tewari and Majumdar 2012). Figure 2 shows the generated AP in the AIS and the regenerated AP in the nodes and bouton. Here, the voltage delay and attenuation resulted from the AP propagation across the myelinated segments. The change in amplitude from the AIS (peak amplitude of 36.53 mV) to the first node of Ranvier (peak amplitude of 46.56 mV) is due to the increase of channel conductances in the nodes. Due to the increase in the voltage-gated channels and the change in their reversal potential, nodal Na^+ current amplifies the axosomatic AP and hyperpolarizes the AP voltage (Kole 2011; Zbili et al. 2016).

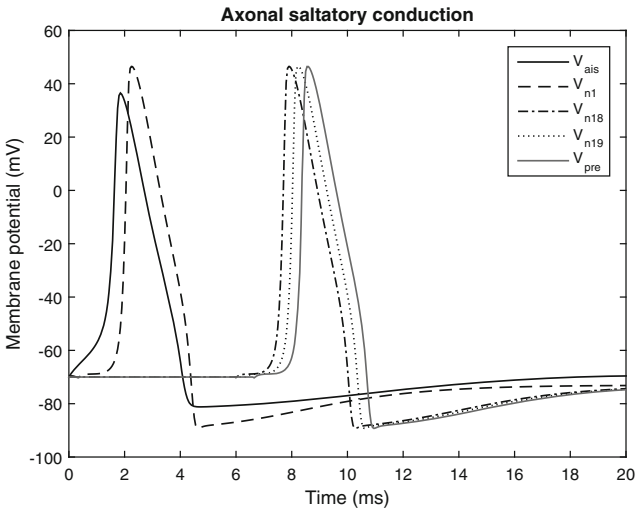

Fig. 2 Axonal saltatory conduction showing the changes on the AP waveform and propagation delay. From the AIS to the first node of Ranvier, there is a 0.33 ms delay in AP arrival; therefore, it takes 6.66 ms before AP reaches the bouton

In this model, the astrocyte is assumed to be covering the synapse and the 19th node as well. Action potential evokes neuronal [Ca^{2+}]; therefore, the frequency of the Ca^{2+} is also the same as that of the input current. The [Ca^{2+}] is the summation of the AP evoked Ca^{2+} and the ER Ca^{2+} fluxes. As presented in Fig. 3, the [Ca^{2+}] fluctuations exhibit probabilistic behavior concurrent with the arrival of AP. The average peak amplitudes of [Ca^{2+}] in the bouton and node were 7511 nM and 4919 nM, respectively. With the same channel conductance and compartment-to-ER ratio, the difference between the amplitudes of bouton [Ca^{2+}] and nodal [Ca^{2+}] is the consequence of the morphometric properties of the compartments.

Figure 4a shows the localized transient [Ca^{2+}] elevations in the astrocyte. These transients are independent from each other, occur rapidly due to the individual Ca2+ stores (Verkhratsky et al. 2016), and are highly variable between cell subcompartments (Handy et al. 2017). Note that the resulting Ca^{2+} dynamics coincide with the experimental studies using mouse hippocampus slices wherein patterns of transients and localized Ca^{2+} events with different sizes and durations were detected in a single astrocyte (Wu et al. 2014; Wu et al. 2018). Spatial quantification of Ca^{2+} by López-Caamal et al. (2014) indicated a local initial [Ca^{2+}]. Then, these Ca^{2+} waves can remain localized or can propagate. Shreds of evidence showed that after initiation, Ca^{2+} waves spread within the cell (Manninen et al. 2018; Ashhad and Narayanan 2018; Semyanov 2018). Figure 4b displays the total intracellular [Ca^{2+}]. Vesicle synthesis in astrocytes is dependent on the sensitivity of the secretory apparatus to the intracellular Ca^{2+} (Verkhratsky et al. 2016). Once the [Ca^{2+}] crosses the threshold with a positive slope, gliotransmitters are released (Fig. 4c). Back to Fig. 4a,

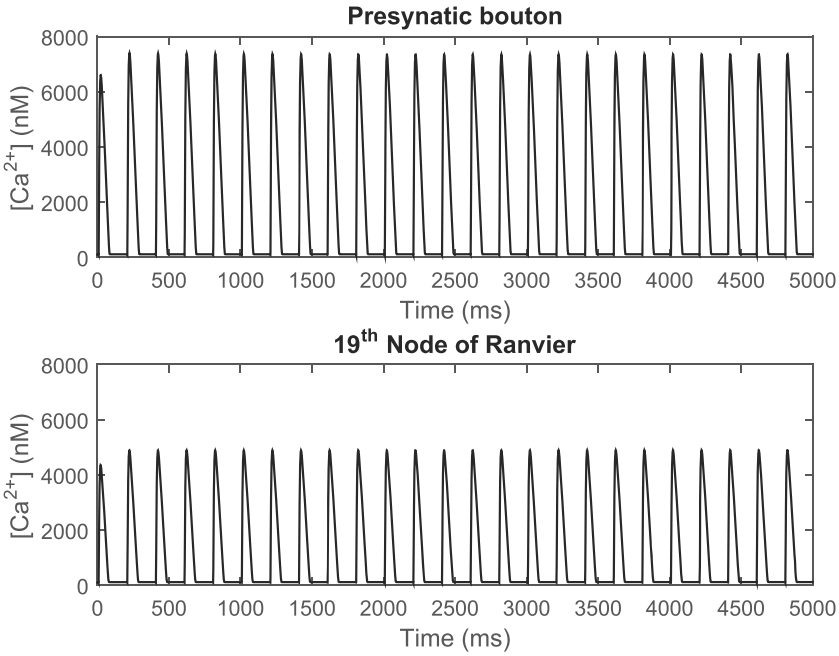

Fig. 3 Calcium dynamics on the presynaptic bouton and node of Ranvier simulated for 5 s

the second elevation of $[Ca^{2+}]_{n19}$ causes the extrasynaptic Glu release. Therefore, even when the synaptic area is silent, the astrocyte might be able to modulate the synaptic transmission by processing signals from the extracellular matrix. However, prolonged delay in Glu release might also be possible. Considering only the $[Ca^{2+}]_{syn}$ dynamics from $t = 36$ s to $t = 40$ s, the extrasynaptic Glu should have been released, but with the addition of $[Ca^{2+}]$, the intracellular $[Ca^{2+}]$ just remained over the threshold, making the vesicle fusion and recycling slower. IP_3 receptors are open during extrasynaptic Glu release, as shown in Fig. 4d. The ER then releases Ca^{2+} into the intracellular area which increases the $[Ca^{2+}]$ elevation peaks (Fig. 4e) in the presynaptic bouton.

The internal Ca^{2+} dynamics (evoked, spontaneous, or both) in the presynaptic compartments determine the vesicle release probability. Figure 5a shows that the fraction of vesicles ready to be released from the bouton into the synaptic cleft is between 0.9249-1, while Fig. 5b presents the corresponding synaptic [Glu]. There were 50 Glu spikes within 50 seconds of simulation. Furthermore, Fig. 5c–d show the fraction of releasable vesicle in the node and the corresponding perinodal [Glu], respectively. Compared to the bouton, the node has a lower release probability, ranging from 0.8621-1. This phenomenon can be attributed to the absence of astrocytic Glu release into the node, as well as to the lower nodal $[Ca^{2+}]$.

The postsynaptic membrane potential is dependent on the amount of synaptic [Glu]. Therefore, the sudden increase in synaptic [Glu] results in a voltage spike in the postsynaptic spine head as shown in the relationship between Figs. 5b and 6a. Here, the successful postsynaptic spikes are those with peak $drivingforce \leq (E_{AMPA} - V_{rest})/2$ (Tønnesen and Nägerl 2016). The spikes in Fig. 6a have an average peak amplitude of -39.57 mV. Synaptic efficacy determines the strength of the connection between the pre- and postsynaptic neurons with respect to time, identified by the transferred mutual information based on the activity patterns of the input and output spike trains (Graupner and Brunel 2010; Hennig 2013; London et al. 2002). The synaptic efficacy of the tripartite synapse under consideration, as shown in Fig. 6b, was computed by obtaining the ratio of the number of successful postsynaptic spikes over the number of presynaptic spikes within a sliding window of 5 seconds. The value of the synaptic efficacy starts to increase from 0.08 to 0.12 at $t = 34$ s, which indicates an increase in the influence of the presynaptic neuron and the astrocyte over the postsynaptic activity (London et al. 2002).

Discussed previously are the electrical and chemical dynamics of a neuron-astrocyte interaction with external sources from the extracellular area. To analyze the effects of these sources, we simulated different neuron-astrocyte configurations (tripartite synapse only, tripartite synapse with one perinodal source, and tripartite synapse with two perinodal sources), 20 times each configuration and each for 50 second simulation time. Table 9 summarizes the astrocytic [Glu] released in the extrasynaptic cleft. Here, as the number of nonsynaptic sites for transient Ca^{2+} increases, the gliotransmitter release is less frequent. However, the period wherein Glu is available in the extrasynaptic area is quite extended, which may denote that the vesicle fusion and recycling process slows down.

Most factors affecting the short term synaptic plasticity are in the presynaptic terminals. These factors are the vesicle release probability and the number of vesicles

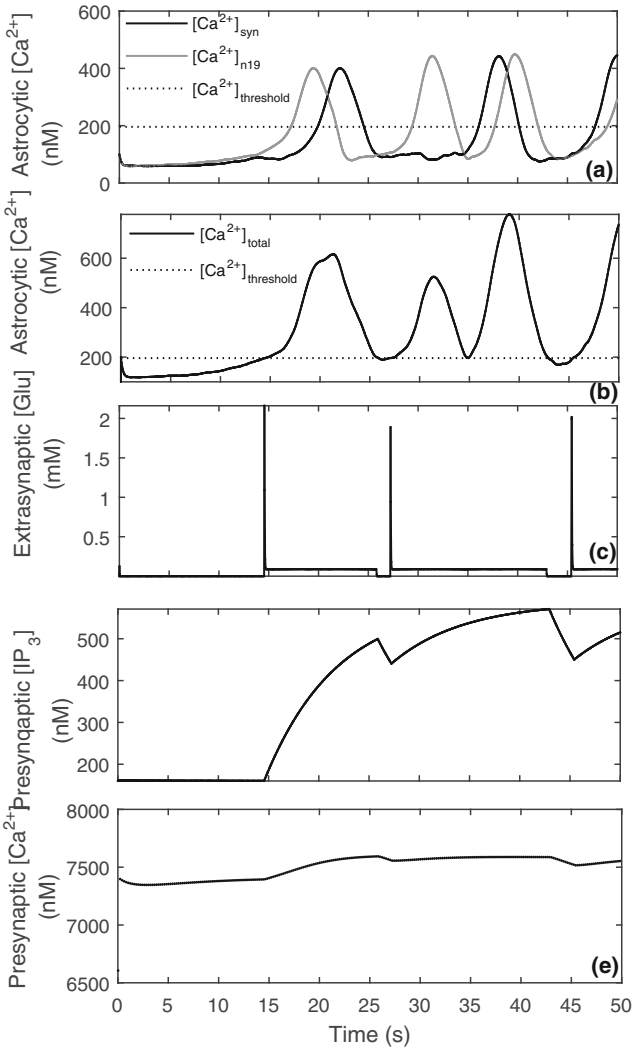

Fig. 4 Calcium and glutamate dynamics. **a** Transient $[Ca^{2+}]$ elevations in the astrocytic compartment covering the synapse and the 19th node. **b** Intracellular $[Ca^{2+}]$ is the summation of the transient Ca^{2+} in the astrocyte. **c** The moment the $[Ca^{2+}]_i$ goes above the threshold, the astrocyte releases gliotransmitters into the extrasynaptic area. **d** IP_3 increases during the presence of extrasynaptic Glu. **e** Increase in $[IP_3]$ causes an increase in the presynaptic Ca^{2+} elevation peaks

available for release. The presynaptic $[Ca^{2+}]$ elevation (which is also dependent on the extrasynaptic [Glu]) increases the probability of vesicle fusion. Moreover, the postsynaptic spiking is dependent on the amount of neurotransmitter in the synaptic cleft, which is then dependent on the number of releasable vesicles in the bouton. We have taken the presynaptic bouton $[Ca^{2+}]$ into account to analyze the effects of the extrasynaptic Glu into the synaptic efficacy. The mean presynaptic $[Ca^{2+}]$ peaks increase as the astrocytic $[Ca^{2+}]$ rises, as shown in Fig. 7a. The ER utilizes the extrasynaptic Glu for Ca^{2+} release via the opening of IP_3Rs. Figure 7b shows the mean $[IP_3]$ for each configuration. The extended period of availability of extrasynaptic Glu causes the IP_3 dynamics to reach equilibrium. Neurotransmitter release is a stochastic process that varies the postsynaptic membrane potential spiking pattern over time. The fundamental quantity in neural circuits that describes these variations is called the synaptic efficacy or strength (Hennig 2013). In Fig. 7c, the mean synaptic efficacy per DT plot for each configuration shows that the model wherein the astrocyte has no perinodal [Glu] source exhibits the least synaptic efficacy. The addition of perinodal sources seems to increase the synaptic strength. However, an extremely high concentration of intracellular Ca^{2+} leads to an abnormal extrasynaptic [Glu] (Barros and Dey 2018) (as shown in Table 9).

The results of the simulation and the changes in the neuron-astrocyte dynamics during the addition of extrasynaptic transmitter sites have constructive and destructive implications to neuronal information processing. Neuron-astrocyte interactions support neural firing and synchronization, and synaptic coordination (Amiri et al. 2013; Gordleeva et al. 2012). However, according to Deplanque (2009), overload in Glu within the synaptic space causes excitotoxic detrimental effects to the postsynaptic spine head by exaggerating the activation of its receptors. The impairment of such glial-neuronal interaction (consisting of perinodal astrocytic components) may result in schizophrenia such as shown in the pathophysiological study conducted by Mitterauer (2014). Neurodegenerative diseases, such as Alzheimer, are caused when astrocyte Ca^{2+} signaling is altered (Shigetomi et al. 2016). On the contrary, the inadequacy in Glu may cause the severity of Alzheimer's disease. Therefore, during synaptic transmission, synaptic Glu insufficiency can be avoided by the additional extrasynaptic transmitter sites provided by the axon-astrocyte interaction.

4 Discussion

Advances in neuron-astrocyte researches broaden our perception of the complexity of brain processes. State-of-the-art imaging techniques challenge the present concept of the tripartite synapse, where information flows from the presynaptic to the postsynaptic component with astrocytic influences on plasticity. We extended the tripartite synapse model presented by Tewari and Majumdar by incorporating nonsynaptic elements through axon-astrocyte interaction for the following reasons. (1) Information transfer is not only confined in the synapse and can be an intercellular process. Astrocytic mGluRs, distributed heterogeneously throughout the cell body, react to extracellular Glu. A single protoplasmic astrocyte can, therefore, sense molecular signals from the neuronal elements within its domain. (2) The vesicular release also occurs in the soma, unmyelinated axon, and varicosities. Adjacent astrocytic processes sense these

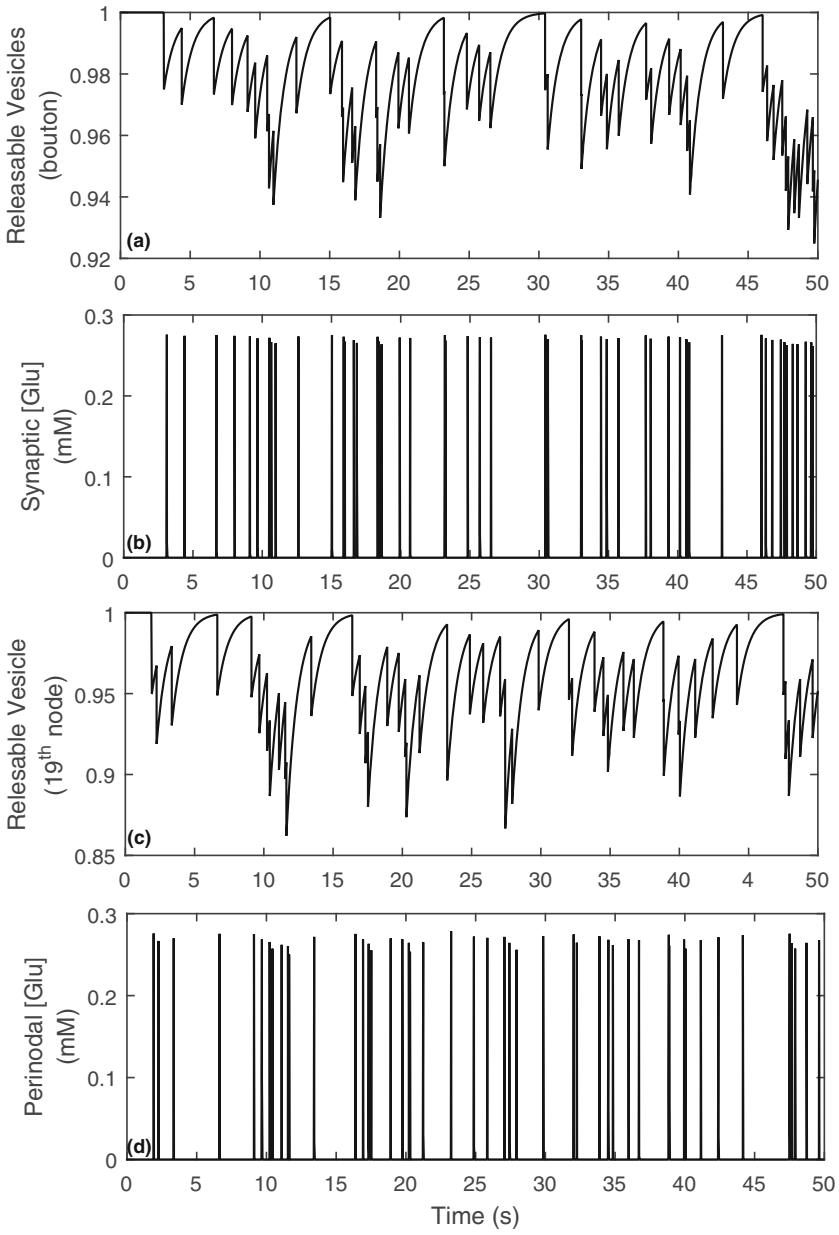

Fig. 5 Synaptic and perinodal glutamate. **a** The fraction of releasable vesicles in the bouton has a maximum value of 1 and a minimum value of 0.9249. **b** The Glu spikes are dependent on the fraction of vesicles ready to be released from the bouton. Within 50 seconds, there were 50 vesicle releases. **c** The node of Ranvier can release neurotransmitter as well. The fraction of releasable vesicles in the node lies between 0.8621-1. **d** The node was able to release neurotransmitters 49 times during 50 s of recurring stimulation

signals, in turn, recognizing the activity of neighboring neurons or networks. (3) Compartmentalization of neuronal and astrocytic Ca^{2+} dynamics is probable. In the neuron, the cell morphology, the expression of ionic channels, the distribution of Ca^{2+} stores, and the behavior of AP means that intracellular [Ca^{2+}] varies across the neuron. Supported by the ER, astrocytic Ca^{2+} dynamics are transient and localized, indicating individual processes in each locality. With these, we presented a model of neuron-astrocyte interaction extending the tripartite synapse by incorporating saltatory conduction along the myelinated axon, nonsynaptic neurotransmitter release, perinodal astrocytic compartments, and integration of transient astrocytic [Ca^{2+}] for gliotransmitter release.

Previous models assumed that AP generated in the AIS reaches the axon terminals without delay or decay by considering the axon as one compartment. We showed that even though myelination promotes rapid conduction, signal delay still occurs. Besides, the AP waveform changes due to the different expression of ionic channels in the nodes and the AIS. Therefore, we considered the axonal length as a sequence of compartments representing the nodes and myelinated segments. By doing so, we were able to insert perinodal processes that are independent of the synapse. We described its dynamics starting from the nodal [Ca^{2+}] elevations during saltatory conduction, followed by the unmyelinated axonal vesicular release, then the Glu dynamics in the perinodal area, to the activation of

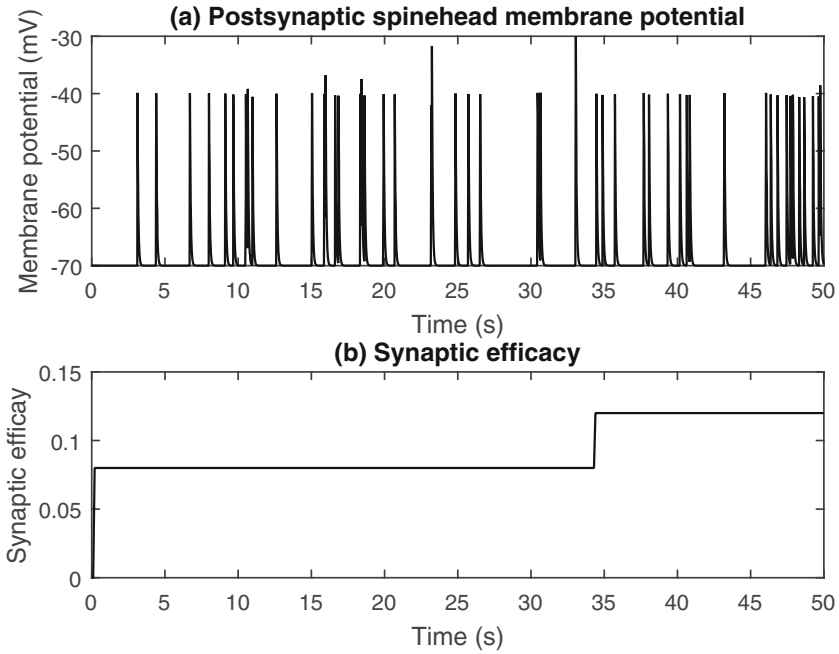

Fig. 6 Postsynaptic membrane potential and synaptic efficacy. **a** The postsynaptic membrane potential of the dendritic head is dependent on the synaptic [Glu]. The number of spikes coincides with the synaptic Glu spikes with an average peak amplitude of –39.57 mV. **b** The synaptic efficacy is stable when t is between 0 and 34 s at 0.08, then increases to 0.12

perisynaptic astrocytic mGluRs, and finally, the perinodal astrocytic Ca^{2+} dynamics.

Additionally, we presented localization of astrocytic Ca^{2+} dynamics in the perisynaptic and perinodal compartments. The stochastic nature of neurotransmitter release, as well as the spatial variation in extracellular [Glu] surrounding the astrocyte, influences Ca^{2+} transients. Here, we assumed a linear summation of transient [Ca^{2+}] in the soma. The total intracellular [Ca^{2+}] determines the [Glu] into the perisynaptic cleft. If astrocyte influences thousands of neuronal elements within its territory, it suggests that the individual astrocytic processes in its branch and branchlets and its somata form a new level of functional integration. We recommend further biophysical investigation and model formulation on astrocytes viewed as a compartmentalized system, similar to neurons, rather than a point process.

We also analyzed the influence of such interaction on synaptic plasticity. The additional nonsynaptic Glu sources boost the intracellular astrocytic calcium [Ca^{2+}], which in turn improves synaptic efficacy. Furthermore, as the extrasynaptic [Glu] increases, indirectly, presynaptic Ca^{2+} stored in the ER will be depleted. Excessive Glu in the synaptic area exaggeratedly activates postsynaptic receptors damaging neurons.

Rossi (2015) suggested that the intercellular coordination of elements within the astrocytic domain indicates a new layer of functional integration that does not entirely include synaptic networks. Here, we present a model of a tripartite synapse whose dynamics are not only dependent on the tripartite area. This model is not restricted to the perinodal astrocytic process and may be varied to represent perineuronal astrocytic processes, as neuron-astrocyte signaling is not only synapse-specific but cell- and circuit-specific as well (Durkee and Araque 2018).

We presented a model of intercellular communication between a neuron and astrocyte that includes synaptic and nonsynaptic processes. In the present wave of researches on astrocytic processes, conflicting views on gliotransmission, being an artifact or reality, arise. Over the years, controversies regarding gliotransmission emerge, whether if it is an innate astrocytic process or a consequence of pharmacological stimulations (Nedergaard and Verkhratsky 2012; Sloan and Barres 2014). Fiacco and McCarthy (2018) deduced that gliotransmission is not a physiological mechanism, but the result of observing cultured astroglia *in vitro*, thus it does not affect short- and long-term plasticity. (Savtchouk and Volterra 2018) contradicted the "negative" evidence on astrocytic Ca^{2+} waves, explaining that this concept is due to the oversimplifications of data collection techniques and presumptions on the interpretation of results. A century ago, Santiago Ramon y Cajal expressed that the real purpose of glial cells would only be known when a direct method of studying them is available (Kettenmann and Verkhratsky 2008). Heterogeneity and complexity of astrocytic mechanisms lead to divergence in conclusions on the exact role of astrocyte in information transfer. Until such time that researchers arrive at a coherent view, differences in perception imply that our current knowledge of astrocytic mechanisms is still inadequate. Moreover, interaction between local [Ca^{2+}] elevations and their propagation through the

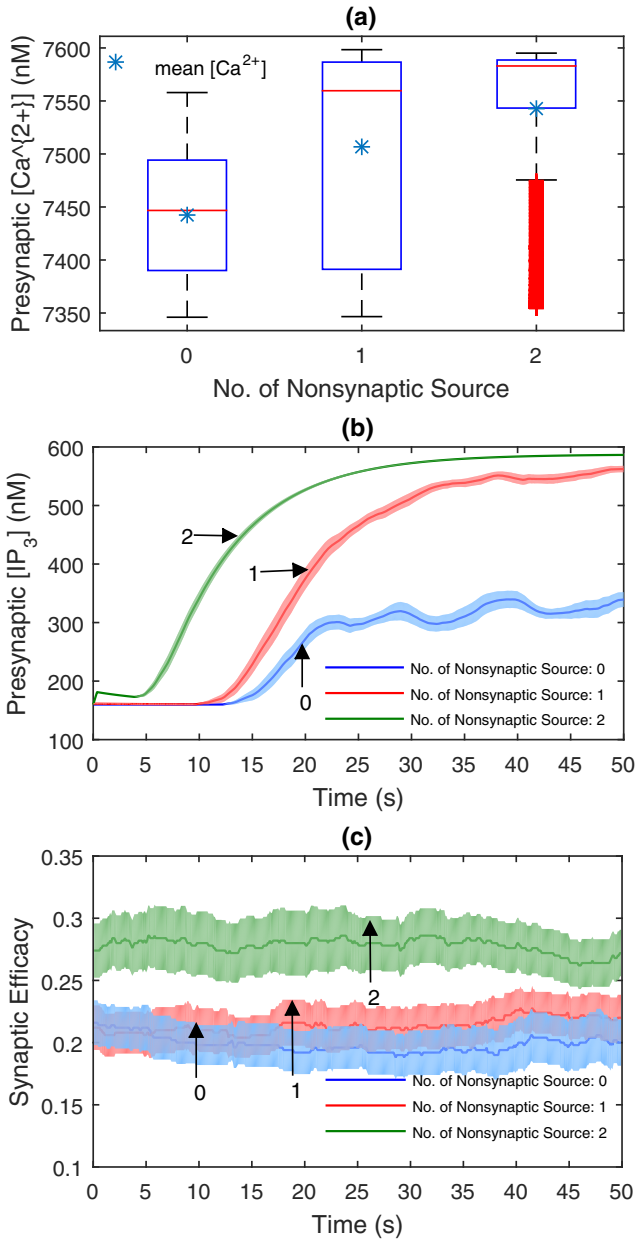

Fig. 7 Comparison of synaptic efficacy. **a** As the number of nonsynaptic sources increases, the astrocytic $[Ca^{2+}]$ rises, therefore heightening the presynaptic Ca^{2+} peaks. **b** The $[Ca^{2+}]$ elevates due to the opening of IP_3Rs due to the extrasynaptic Glu. The solid line indicates the change of mean synaptic efficacy with time for the three model configurations, while the shaded area is the corresponding standard error. **c** The comparison of synaptic efficacy between the three configurations shows that the increasing calcium stores releasing astrocytic Ca^{2+} enhance synaptic efficacy

Table 9 Summary of extrasynaptic glutamate

No. of Sources	Average No. of Glutamate Spikes (50-sec Stimulation)	Average Time Before First Spike (s)	Average [Glu] Peak (mM)	Average Period of [Glu] elevation (s)
0	3.4	17.40	1.7414	4.56
1	2.35	14.5	1.7955	11.85
2	1.05	6.05	2.1712	$\geq$ 44.04

cell and the astrocytic network are currently inconclusive. Future experimental and methodological advances will provide clarifications of these issues.

5 Conclusion

The heterogeneity of mGluRs expression and the morphological complexity of the astrocyte, along with various sources of extracellular Glu within the astrocytic territory, create local sites for $[Ca^{2+}]$ elevations. In this study, we have presented a biologically plausible tripartite synapse model and extended it by incorporating axon-astrocyte interaction that represents uncanonical components for signal transmission. We investigated its Ca^{2+} dynamics and found that the summation of astrocytic local and transient $[Ca^{2+}]$, which increases the total intracellular $[Ca^{2+}]$, may impede the vesicular fusion and recycling process. This impediment results in Glu prolongation in the extrasynaptic cleft. In the short-term, this may increase synaptic efficacy. However, the continuous source of extrasynaptic Glu causes depletion of Ca2+ stored in the presynaptic ER and then overactivation of postsynaptic receptors. Therefore, in the long-term, this may cause detrimental effects to the pre- and postsynaptic neurons. Further investigation of Ca^{2+} dynamics is necessary to clarify the exact function of astrocyte in intercellular and internetwork communication.

Acknowledgements The authors would also like to acknowledge Shivendra G. Tewari and Kaushik Kumar Majumdar for sharing the Matlab code essential for this study.

Compliance with Ethical Standards

Conflict of interests The authors declare that they have no conflict of interest.

References

Abbracchio, M.P., Burnstock, G., Verkhratsky, A., Zimmermann, H. (2009). Purinergic signalling in the nervous system: an overview. *Trends in Neurosciences*, *32*(1), 19–29.

Amiri, M., Hosseinmardi, N., Bahrami, F., Janahmadi, M. (2013). Astrocyte-neuron interaction as a mechanism responsible for generation of neural synchrony: a study based on modeling and experiments. *Journal of Computational Neuroscience*, *34*(3), 489–504.

Arancibia-Carcamo, I.L., Ford, M.C., Cossell, L., Ishida, K., Tohyama, K., Attwell, D. (2017). Node of ranvier length as a potential regulator of myelinated axon conduction speed. *Elife*, *6*, e23,329.

Ashhad, S., & Narayanan, R. (2018). Stores, channels, glue, and trees: active glial and active dendritic physiology. *Molecular Neurobiology*, 1–22.

Babbs, C.F., & Shi, R. (2013). Subtle paranodal injury slows impulse conduction in a mathematical model of myelinated axons. *PLoS One*, *8*(7), e67,767.

Barros, M., & Dey, S. (2018). Feed-forward and feedback control in astrocytes for ca2+-based molecular communications nanonetworks. *IEEE/ACM Transactions on Computational Biology and Bioinformatics*.

Bazargani, N., & Attwell, D. (2016). Astrocyte calcium signaling: the third wave. *Nature Neuroscience*, *19*(2), 182.

Bezzi, P., & Volterra, A. (2014). Imaging exocytosis and recycling of synaptic-like microvesicles in astrocytes. *Cold Spring Harbor Protocols*, *2014*(5), pdb–prot081,711.

Bogatov, N., Grigoryan, L., Ponetaeva, E., Sinisyn, A. (2014). Calculation of action potential propagation in nerve fiber. *Progress in Biophysics and Molecular Biology*, *114*(3), 170–174.

Bucher, D., & Goaillard, J.M. (2011). Beyond faithful conduction: short-term dynamics, neuromodulation, and long-term regulation of spike propagation in the axon. *Progress in Neurobiology*, *94*(4), 307–346.

Bushong, E.A., Martone, M.E., Jones, Y.Z., Ellisman, M.H. (2002). Protoplasmic astrocytes in ca1 stratum radiatum occupy separate anatomical domains. *Journal of Neuroscience*, *22*(1), 183–192.

Bushong, E.A., Martone, M.E., Ellisman, M.H. (2004). Maturation of astrocyte morphology and the establishment of astrocyte domains during postnatal hippocampal development. *International Journal of Developmental Neuroscience*, *22*(2), 73–86.

Butt, A.M. (2011). Atp: a ubiquitous gliotransmitter integrating neuron–glial networks. In *Seminars in cell & developmental biology*, (Vol. 22 pp. 205–213): Elsevier.

Chan, S.C., Mok, S.Y., Ng, D.W.K., Goh, S.Y. (2017). The role of neuron–glia interactions in the emergence of ultra-slow oscillations. *Biological Cybernetics*, *111*(5–6), 459–472.

Choi, M., Ahn, S., Yang, E.J., Kim, H., Chong, Y.H., Kim, H.S. (2016). Hippocampus-based contextual memory alters the morphological characteristics of astrocytes in the dentate gyrus. *Molecular Brain*, *9*(1), 72.

Cinciute, S. (2019). Translating the hemodynamic response: why focused interdisciplinary integration should matter for the future of functional neuroimaging. *PeerJ*, *7*, e6621.

de Juan-Sanz, J., Holt, G.T., Schreiter, E.R., de Juan, F., Kim, D.S., Ryan, T.A. (2017). Axonal endoplasmic reticulum ca 2+ content controls release probability in cns nerve terminals. *Neuron*, *93*(4), 867–881.

De Pittà, M., & Brunel, N. (2016). Modulation of synaptic plasticity by glutamatergic gliotransmission: a modeling study. *Neural Plasticity*, 2016.

De Pittà, M., Brunel, N., Volterra, A. (2016). Astrocytes: orchestrating synaptic plasticity? *Neuroscience*, *323*, 43–61.

Debanne, D., & Rama, S. (2011). Astrocytes shape axonal signaling. *Science of Signal*, *4*(162), pe11–pe11.

Del-Bel, E., & De-Miguel, F.F. (2018). Extrasynaptic neurotransmission mediated by exocytosis and diffusive release of transmitter substances. *Frontiers in Synaptic Neuroscience*, 10.

Deplanque, D. (2009). Maladie d'alzheimer: dualité des effets physiologiques et pathologiques du glutamate. *La Lettre du pharmacologue Supplé,ment*, *23*(4), 13–22.

Ding, X., Zhang, X., Ji, L. (2018). Contribution of calcium fluxes to astrocyte spontaneous calcium oscillations in deterministic and stochastic models. *Applied Mathematical Modelling*, *55*, 371–382.

Durkee, C.A., & Araque, A. (2018). Diversity and specificity of astrocyte-neuron communication. *Neuroscience*.

Dutta, D.J., Woo, D.H., Lee, P.R., Pajevic, S., Bukalo, O., Huffman, W.C., Wake, H., Basser, P.J., SheikhBahaei, S., Lazarevic, V., et al. (2018). Regulation of myelin structure and conduction velocity by perinodal astrocytes. *Proceedings of the National Academy of Sciences*, *115*(46), 11,832–11,837.

English, D.F., McKenzie, S., Evans, T., Kim, K., Yoon, E., Buzsáki, G. (2017). Pyramidal cell-interneuron circuit architecture and dynamics in hippocampal networks. *Neuron*, *96*(2), 505–520.

Evans, R., & Blackwell, K. (2015). Calcium: amplitude, duration, or location? *The Biological Bulletin*, *228*(1), 75–83.

Fiacco, T.A., & McCarthy, K.D. (2018). Multiple lines of evidence indicate that gliotransmission does not occur under physiological conditions. *Journal of Neuroscience*, *38*(1), 3–13.

Fletcher, A. (2016). Nerve cell function and synaptic mechanisms. *Anaesthesia & Intensive Care Medicine*, *17*(4), 199–203.

Ford, M.C., Alexandrova, O., Cossell, L., Stange-Marten, A., Sinclair, J., Kopp-Scheinpflug, C., Pecka, M., Attwell, D., Grothe, B. (2015). Tuning of ranvier node and internode properties in myelinated axons to adjust action potential timing. *Nature Communications*, *6*, 8073.

Freeman, S.A., Desmazieres, A., Fricker, D., Lubetzki, C., Sol-Foulon, N. (2016). Mechanisms of sodium channel clustering and its influence on axonal impulse conduction. *Cellular and Molecular Life Sciences*, *73*(4), 723–735.

Genç, Ö., Dickman, D.K., Ma, W., Tong, A., Fetter, R.D., Davis, G.W. (2017). Mctp is an er-resident calcium sensor that stabilizes synaptic transmission and homeostatic plasticity. *Elife*, *6*, e22,904.

Gordleeva, S.Y., Stasenko, S.V., Semyanov, A.V., Dityatev, A.E., Kazantsev, V.B. (2012). Bi-directional astrocytic regulation of neuronal activity within a network. *Frontiers in Computational Neuroscience*, *6*, 92.

Gordleeva, S.Y., Lebedev, S., Rumyantseva, M., Kazantsev, V.B. (2018). Astrocyte as a detector of synchronous events of a neural network. *JETP Letters*, *107*(7), 440–445.

Graupner, M., & Brunel, N. (2010). Mechanisms of induction and maintenance of spike-timing dependent plasticity in biophysical synapse models. *Frontiers in Computational Neuroscience*, *4*, 136.

Guerra-Gomes, S., Sousa, N., Pinto, L., Oliveira, J.F. (2018). Functional roles of astrocyte calcium elevations: from synapses to behavior. *Frontiers in Cellular Neuroscience*, *11*, 427.

Gulledge, A.T., & Bravo, J.J. (2016). Neuron morphology influences axon initial segment plasticity. *eNeuro*, ENEURO–0085.

Guo, Y., Liu, Z., Yk, C.hen., Chai, Z., Zhou, C., Zhang, Y. (2017). Neurons with multiple axons have functional axon initial segments. *Neuroscience Bulletin*, *33*(6), 641–652.

Halassa, M.M., Fellin, T., Takano, H., Dong, J.H., Haydon, P.G. (2007). Synaptic islands defined by the territory of a single astrocyte. *Journal of Neuroscience*, *27*(24), 6473–6477.

Handy, G., Taheri, M., White, J.A., Borisyuk, A. (2017). Mathematical investigation of ip 3-dependent calcium dynamics in astrocytes. *Journal of Computational Neuroscience*, *42*(3), 257–273.

Heller, J.P., & Rusakov, D.A. (2017). The nanoworld of the tripartite synapse: insights from super-resolution microscopy. *Frontiers in Cellular Neuroscience*, *11*, 374.

Hennig, M.H. (2013). Theoretical models of synaptic short term plasticity. *Frontiers in Computational Neuroscience*, *7*, 45.

Hliatsevich, M.A., Bulai, P.M., Pitlik, T.N., Denisov, A.A., Cherenkevich, S.N. (2015). Design of deterministic model of signal transduction between neuronal cells. *Mathematical Modelling and Analysis*, *20*(1), 76–93.

Hu, X., Yuan, Y., Wang, D., Su, Z. (2016). Heterogeneous astrocytes: active players in cns. *Brain Research Bulletin*, *125*, 1–18.

Jourdain, P., Bergersen, L.H., Bhaukaurally, K., Bezzi, P., Santello, M., Domercq, M., Matute, C., Tonello, F., Gundersen, V., Volterra,

A. (2007). Glutamate exocytosis from astrocytes controls synaptic strength. *Nature Neuroscience*, *10*(3), 331.

Kelso, J.S., Dumas, G., Tognoli, E. (2013). Outline of a general theory of behavior and brain coordination. *Neural Networks*, *37*, 120–131.

Kettenmann, H., & Verkhratsky, A. (2008). Neuroglia: the 150 years after. *Trends in Neurosciences*, *31*(12), 653–659.

Kole, M.H. (2011). First node of ranvier facilitates high-frequency burst encoding. *Neuron*, *71*(4), 671–682.

Kole, M.H., & Brette, R. (2018). The electrical significance of axon location diversity. *Current Opinion in Neurobiology*, *51*, 52–59.

Kuznetsov, I., & Kuznetsov, A. (2017). How dense core vesicles are delivered to axon terminals–a review of modeling approaches. In *Modeling of microscale transport in biological processes* (pp. 335–352). Elsevier.

Li, J.J., Du, M.M., Wang, R., Lei, J.Z., Wu, Y. (1650). Astrocytic gliotransmitter: diffusion dynamics and induction of information processing on tripartite synapses. *International Journal of Bifurcation and Chaos*, *26*(08), 138.

London, M., Schreibman, A., Häusser, M., Larkum, M.E., Segev, I. (2002). The information efficacy of a synapse. *Nature Neuroscience*, *5*(4), 332.

López-Caamal, F., Oyarzún, D. A., Middleton, R.H., García, M.R. (2014). Spatial quantification of cytosolic ca 2+ accumulation in nonexcitable cells: an analytical study. *IEEE/ACM Transactions on Computational Biology and Bioinformatics (TCBB)*, *11*(3), 592–603.

Manninen, T., Havela, R., Linne, M.L. (2018). Computational models for calcium-mediated astrocyte functions. *Frontiers in Computational Neuroscience*, *12*, 14.

Manninen, T., Havela, R., Linne, M.L. (2019). Computational models of astrocytes and astrocyte–neuron interactions: characterization, reproducibility, and future perspectives. In *Computational glioscience* (pp. 423–454): Springer.

Mirzakhalili, E., Epureanu, B.I., Gourgou, E. (2018). A mathematical and computational model of the calcium dynamics in caenorhabditis elegans ash sensory neuron. *PloS One*, *13*(7), e0201,302.

Mitterauer, B.J. (2014). Pathophysiology of schizophrenia based on impaired glial-neuronal interactions. *Open Journal of Medical Psychology*, *3*(02), 126.

Modchang, C., Nadkarni, S., Bartol, T.M., Triampo, W., Sejnowski, T.J., Levine, H., Rappel, W.J. (2010). A comparison of deterministic and stochastic simulations of neuronal vesicle release models. *Physical Biology*, *7*(2), 026,008.

Namazi, H., & Kulish, V.V. (2013). A mathematical based calculation of a myelinated segment in axons. *Computers in Biology and Medicine*, *43*(6), 693–698.

Nazari, S., Faez, K., Amiri, M., Karami, E. (2015). A digital implementation of neuron–astrocyte interaction for neuromorphic applications. *Neural Networks*, *66*, 79–90.

Nedergaard, M., & Verkhratsky, A. (2012). Artifact versus reality—how astrocytes contribute to synaptic events. *Glia*, *60*(7), 1013–1023.

Nelson, A.D., & Jenkins, P.M. (2017). Axonal membranes and their domains: assembly and function of the axon initial segment and node of ranvier. *Frontiers in Cellular Neuroscience*, *11*, 136.

of Notre Dame, U. (2004). The electrical system of the body. In *Physics in medicine* (pp. 224–242): Elsevier.

Perea, G., Sur, M., Araque, A. (2014). Neuron-glia networks: integral gear of brain function. *Frontiers in Cellular Neuroscience*, *8*, 378.

Pissadaki, E.K., Sidiropoulou, K., Reczko, M., Poirazi, P. (2010). Encoding of spatio-temporal input characteristics by a ca1 pyramidal neuron model. *PLoS Computational Biology*, *6*(12), e1001,038.

Poliak, S., & Peles, E. (2003). The local differentiation of myelinated axons at nodes of ranvier. *Nature Reviews Neuroscience*, *4*(12), 968.

Robertson, J.M. (2013). Astrocyte domains and the three-dimensional and seamless expression of consciousness and explicit memories. *Medical Hypotheses*, *81*(6), 1017–1024.

Rossi, D. (2015). Astrocyte physiopathology: at the crossroads of intercellular networking, inflammation and cell death. *Progress in Neurobiology*, *130*, 86–120.

Sasaki, T. (2013). The axon as a unique computational unit in neurons. *Neuroscience Research*, *75*(2), 83–88.

Sasaki, T., Matsuki, N., Ikegaya, Y. (2011). Action-potential modulation during axonal conduction. *Science*, *331*(6017), 599–601.

Savtchouk, I., & Volterra, A. (2018). Gliotransmission: beyond black-and-white. *Journal of Neuroscience*, *38*(1), 14–25.

Semyanov, A. (2018). Spatiotemporal pattern of ca2+ activity in astrocytic network. *Cell Calcium*.

Shigetomi, E., Patel, S., Khakh, B.S. (2016). Probing the complexities of astrocyte calcium signaling. *Trends in Cell Biology*, *26*(4), 300–312.

Sims, R.E., Butcher, J.B., Parri, H.R., Glazewski, S. (2015). Astrocyte and neuronal plasticity in the somatosensory system. *Neural Plasticity*, 2015.

Sloan, S.A., & Barres, B.A. (2014). Looks can be deceiving: reconsidering the evidence for gliotransmission. *Neuron*, *84*(6), 1112–1115.

Sosunov, A.A., Wu, X., Tsankova, N.M., Guilfoyle, E., McKhann, G.M., Goldman, J.E. (2014). Phenotypic heterogeneity and plasticity of isocortical and hippocampal astrocytes in the human brain. *Journal of Neuroscience*, *34*(6), 2285–2298.

Tewari, S., & Parpura, V. (2013). A possible role of astrocytes in contextual memory retrieval: an analysis obtained using a quantitative framework. *Frontiers in Computational Neuroscience*, *7*, 145.

Tewari, S.G., & Majumdar, K.K. (2012). A mathematical model of the tripartite synapse: astrocyte-induced synaptic plasticity. *Journal of Biological Physics*, *38*(3), 465–496.

Tønnesen, J., & Nägerl, U.V. (2016). Dendritic spines as tunable regulators of synaptic signals. *Frontiers in Psychiatry*, *7*, 101.

Trueta, C., & De-Miguel, F.F. (2012). Extrasynaptic exocytosis and its mechanisms: a source of molecules mediating volume transmission in the nervous system. *Frontiers in Physiology*, *3*, 319.

Ventura, R., & Harris, K.M. (1999). Three-dimensional relationships between hippocampal synapses and astrocytes. *Journal of Neuroscience*, *19*(16), 6897–6906.

Verkhratsky, A., Matteoli, M., Parpura, V., Mothet, J.P., Zorec, R. (2016). Astrocytes as secretory cells of the central nervous system: idiosyncrasies of vesicular secretion. *The EMBO Journal*, *35*(3), 239–257.

Vizi, E.S., & Kiss, J.P. (1998). Neurochemistry and pharmacology of the major hippocampal transmitter systems: synaptic and nonsynaptic interactions. *Hippocampus*, *8*(6), 566–607.

Volterra, A., & Meldolesi, J. (2005). Astrocytes, from brain glue to communication elements: the revolution continues. *Nature Reviews Neuroscience*, *6*(8), 626.

Volterra, A., Liaudet, N., Savtchouk, I. (2014). Astrocyte ca 2+ signalling: an unexpected complexity. *Nature Reviews Neuroscience*, *15*(5), 327.

Wade, J.J., McDaid, L.J., Harkin, J., Crunelli, V., Kelso, J.S. (2011). Bidirectional coupling between astrocytes and neurons mediates learning and dynamic coordination in the brain: a multiple modeling approach. *PloS One*, *6*(12), e29,445.

Wallach, G., Lallouette, J., Herzog, N., De Pittà, M., Jacob, E.B., Berry, H., Hanein, Y. (2014). Glutamate mediated astrocytic

filtering of neuronal activity. *PLoS Computational Biology*, *10*(12), e1003,964.

Woo, B., & Choi, J. (2007). Reduced model and simulation of myelinated axon using eigenfunction expansion and singular perturbation. *Computers in Biology and Medicine*, *37*(8), 1148–1154.

Wu, Y.W., Tang, X., Arizono, M., Bannai, H., Shih, P.Y., Dembitskaya, Y., Kazantsev, V., Tanaka, M., Itohara, S., Mikoshiba, K., et al. (2014). Spatiotemporal calcium dynamics in single astrocytes and its modulation by neuronal activity. *Cell Calcium*, *55*(2), 119–129.

Wu, Y.W., Gordleeva, S., Tang, X., Shih, P.Y., Dembitskaya, Y., Semyanov, A. (2018). Morphological profile determines the frequency of spontaneous calcium events in astrocytic processes. *Glia*.

Yamada, R., & Kuba, H. (2016). Structural and functional plasticity at the axon initial segment. *Frontiers in Cellular Neuroscience*, *10*, 250.

Ye, H., & Ng, J. (2018). Shielding effects of myelin sheath on axolemma depolarization under transverse electric field stimulation. *PeerJ*, *6*, e6020.

Zbili, M., Rama, S., Debanne, D. (2016). Dynamic control of neurotransmitter release by presynaptic potential. *Frontiers in Cellular Neuroscience*, *10*, 278.

Zhou, B., Zuo, Y.X., Jiang, R.T. (2019). Astrocyte morphology: diversity, plasticity, and role in neurological diseases. *CNS Neuroscience & Therapeutics*, *25*(6), 665–673.

Ziskin, J.L., Nishiyama, A., Rubio, M., Fukaya, M., Bergles, D.E. (2007). Vesicular release of glutamate from unmyelinated axons in white matter. *Nature Neuroscience*, *10*(3), 321.